Boosting Z-scheme water splitting via increasing electron transport by manipulating multiple redox-active sites and potentials in metal hexacyanoferrate modifiers

Journal:	*EES Solar*
Manuscript ID	EL-ART-04-2026-000066.R1
Article Type:	Paper
Date Submitted by the Author:	15-May-2026
Complete List of Authors:	Ninomiya, Harutaka; Kyoto University, Department of Energy and Hydrocarbon Chemistry Tomita, Osamu; Kyoto University, Department of Energy and Hydrocarbon Chemistry Nakada, Akinobu; Kyoto University, Department of Energy and Hydrocarbon Chemistry Suzuki, Hajime; Kyoto University, Department of Energy and Hydrocarbon Chemistry; PRESTO Haruki, Rie; High Energy Accelerator Research Organization, Photon Factory Nozawa, Shunsuke; High Energy Accelerator Research Organization, Photon Factory Abe, Ryu; Kyoto University, Department of Energy and Hydrocarbon Chemistry

View Article Online
DOI: 10.1039/D6EL00066E

Broader Context Statement

Water and sunlight are abundant and globally available resources, making solar water splitting an attractive route to sustainable hydrogen production. Among the proposed approaches, particulate Z-scheme systems are particularly appealing because they can enable scalable solar H_2 production using dispersed semiconductor materials and simple reactor configurations. However, their performance is often limited not only by the semiconductor photocatalysts themselves, but also by inefficient interfacial electron transfer between aqueous redox mediators and photocatalyst surfaces. Nevertheless, the design of cocatalysts for redox-mediator oxidation has received far less attention than that for water reduction or oxidation. In this work, we show that metal hexacyanoferrates can serve as tunable mediator-oxidation cocatalysts, and that their redox potentials critically govern forward charge extraction and backward electron transfer. We further demonstrate that high-entropy compositional design improves durability while retaining function. Together, these findings establish a redox-potential-based design principle for mediator oxidation and provide a general framework for engineering interfacial redox selectivity and durability in solar-to-fuel conversion systems.

View Article Online
DOI: 10.1039/D6EL00066E

ARTICLE

Boosting Z-scheme water splitting via increasing electron transport by manipulating multiple redox-active sites and potentials in metal hexacyanoferrate modifiers

Received 00th January 20xx,
Accepted 00th January 20xx

DOI: 10.1039/x0xx00000x

Harutaka Ninomiya,[a] Osamu Tomita,[a] Hajime Suzuki,[a,b] Akinobu Nakada,[a] Rie Haruki,[c] Shunsuke Nozawa,[c] and Ryu Abe*[a]

Metal hexacyanoferrates (MHCFs) are attractive cocatalysts for Z-scheme water splitting owing to their tunable redox properties at the C-coordinated Fe^{III}/Fe^{II} sites, enabling efficient electron transfer from shuttle redox mediators. MHCFs can incorporate multiple transition metal centers through ambidentate cyanide ligands; however, rational design principles for utilizing redox-active metals at the N-coordinated sites remain unclear. Herein, we show that photocatalytic H_2 evolution is governed by the relative alignment of redox potentials of MHCF modifiers and aqueous electron donors. A series of MHCFs comprising redox-active metals (i.e., Mn, Fe, Co, Cu) and redox-inactive metals (i.e., In, Ni) were loaded on Rh-Cr mixed-oxide-modified TaON, and their electrochemical properties were correlated with photocatalytic H_2 evolution using electron donors with different electron-donating ability. MHCFs containing redox-active metal species with redox potential significantly more negative than those of the electron donors (e.g., the N-coordinated $Fe^{III/II}$ in FeHCF, and $Cu^{II/I}$ in CuHCF) suppressed photocatalytic activity due to backward electron transfer (reduction via photoexcited electrons), whereas MnHCF, with both $Mn^{III/II}$ and $Fe^{III/II}$ potentials more positive than the donors, exhibited the highest activity. Furthermore, the incorporation of multiple metals in a Mn-based high-entropy MHCF ($K_2Mn_{0.4}Fe_{0.15}Co_{0.15}Ni_{0.15}Cu_{0.15}[Fe(CN)_6]$) improved durability while maintaining appropriate redox potentials, yielding a higher amount of gas evolution compared with MnHCF in Z-scheme water splitting. These findings provide a design strategy for multi-redox-active MHCF cocatalysts, highlighting that the optimal choice and tuning of metal sites can achieve both high efficiency and durability in water splitting systems.

Introduction

Photocatalytic water splitting using particulate semiconductors is attracting attention for implementation in large-scale H_2 production.[1] A Z-scheme-type water splitting (Zs-WS) system can be promising from the perspective of effective utilization of visible light, which accounts for the majority of solar energy.[2] Zs-WS systems basically consist of three components: a H_2-evolving photocatalyst (HEP), an O_2-evolving photocatalyst (OEP), and a shuttle redox couple. The shuttle redox couple is expected to transfer excited electrons from OEP to HEP, as illustrated in **Figure 1**.[2,3] Improving the overall efficiency of Zs-WS requires not only improvements in semiconductor bulk properties[4–6] but also promotion of four forward reactions (i.e., (1) reduction of water (or H^+), (2) oxidation of reductant (Red) on HEP, (3) reduction of oxidant (Ox), and (4) oxidation of water (or OH^-) on OEP), as well as suppression of two backward reactions (i.e., reduction of Ox on HEP and oxidation of Red on OEP). Among the four forward reactions, the promotion of H_2 evolution (1) and O_2 evolution (4) has been extensively studied and achieved by loading effective cocatalysts (e.g., Pt, CoO_x, IrO_2) on the photocatalyst surfaces; most have been developed based on the knowledge accumulated from electrolysis.[7–9] Also, facet-selective deposition of such cocatalysts spatially separates reduction and oxidation sites, thereby promoting forward interfacial charge transfer while suppressing charge recombination.[9,10] Conversely, the promotion of the other two forward reactions with the redox couple (2), (3) has not been sufficiently addressed, despite their importance in activating and/or boosting redox reactions on each photocatalyst and resulting Zs-WS.[9,11–17] Although previous studies revealed that cocatalysts such as PtO_x and RuO_2 (or their analogues) effectively promoted the reduction of Ox (e.g., IO_3^-, Fe^{3+}), the effective promoted oxidation of their Red (e.g., I^-, Fe^{2+}) has seldom been reported.[12,17,18]

[a] *Department of Energy and Hydrocarbon Chemistry, Graduate School of Engineering, Kyoto University, Nishikyo-ku, Kyoto 615-8510, Japan. E-mail: ryu-abe@scl.kyoto-u.ac.jp*
[b] *Precursory Research for Embryonic Science and Technology (PRESTO), Japan Science and Technology Agency (JST), Kawaguchi, Saitama 332-0012, Japan*
[c] *Photon Factory (PF), Institute of Materials Structure Science (IMSS), High Energy Accelerator Research Organization (KEK), Tsukuba, Ibaraki 305-0801, Japan*
Supplementary Information available: [details of any supplementary information available should be included here]. See DOI: 10.1039/x0xx00000x

View Article Online
DOI: 10.1039/D6EL00066E

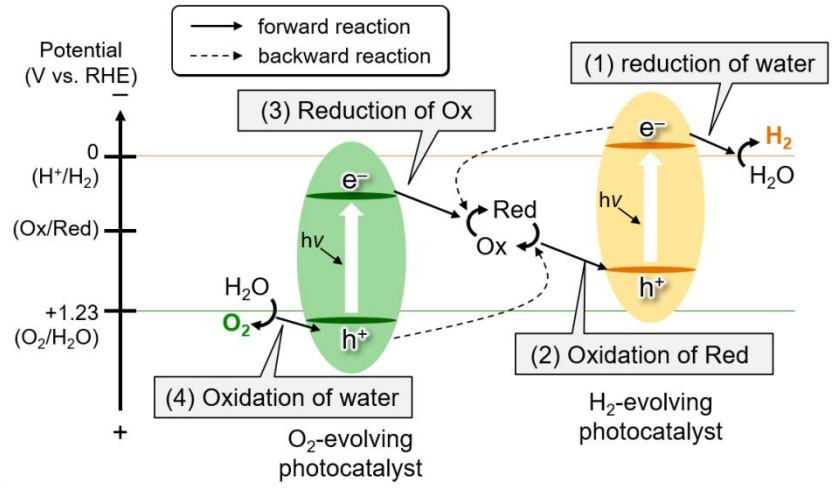

Figure 1. Schematic of Z-scheme water splitting (Zs-WS).

We have previously demonstrated that some metal hexacyanoferrates (MHCFs) function as effective cocatalysts for boosting the oxidation of such reductants and eventually promote H_2 evolution on various HEPs (e.g., CdS, $ZnIn_2S_4$, TaON).[19–22] MHCFs comprise a three-dimensional cubic framework in which Fe_C and transition metals (M_N) are octahedrally coordinated to the carbon and nitrogen, respectively, of the cyanide ligand (**Figure 2(a)**).[23,24] MHCFs offer structural tunability, enabling the modulation of various important physicochemical properties as a cocatalyst, such as the redox potential of Fe_C by varying M_N species.[24–27] The Fe_C^{II} species contained in MHCFs (e.g., InHCF, NiHCF) are oxidized by photogenerated holes, generating Fe_C^{III} species that effectively oxidize Red (i.e., electron donors) such as $[Fe^{II}(CN)_6]^{4-}$ and Fe^{2+}.[19,20,28] The driving force for the oxidation of electron donors can be tuned depending on the redox potential of $Fe_c^{III/II}$ by varying the M_N.[28] This redox-based function of MHCFs promotes H_2 evolution and expands the choice of HEPs available for Zs-WS.[15] Furthermore, introducing redox-active M_N (e.g., $Mn^{III/II}$, $Fe^{III/II}$, $Co^{III/II}$, $Cu^{II/I}$), instead of inactive species (e.g., In^{III}, Ni^{II}), enables such MHCFs to exhibit multiple redox behaviors based on both Fe_C and M_N sites.[29–31] In addition, the design of MHCFs to incorporate multiple metal species into the M_N site generates the so-called high-entropy MHCF.[32–34] However, the attractive potential of such MHCFs with multiple redox species for photocatalytic water splitting has not been explored to date.

This study investigated how the redox properties of MHCF cocatalysts vary depending on the M_N species, with particular emphasis on the influence of redox-active M_N species on the promotion of oxidation, coupled with V-substituted polyoxometalates (V-POMs) as potential-tunable redox couples.[19–22,35–38] Each MHCF was loaded onto an HEP (i.e., Rh-Cr mixed oxide (RCO)/TaON), and photocatalytic H_2 evolution was evaluated using two types of V-POMs with different redox potentials, $[SiV^{IV}W_{11}O_{40}]^{6-}$ (SiV^{IV}) and $[BV^{IV}W_{11}O_{40}]^{7-}$ (BV^{IV}), as an electron donor (**Figure 2(b)**). The impact of MHCF modifiers on H_2 evolution, their stability during redox cycling, and the resultant Zs-WS were thoroughly examined.

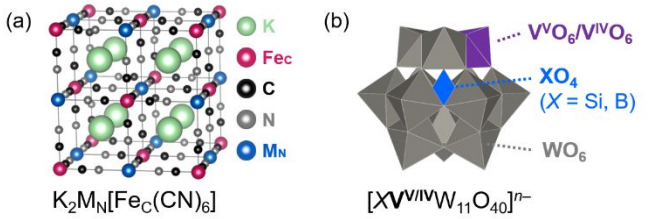

Figure 2. Structure of (a) MHCF ($K_2M^{II}[Fe^{II}(CN)_6]$) and (b) V-POMs.

Experimental

Details of the reagents are provided in the Supplementary Information (SI).

Synthesis of MHCF

MHCFs were synthesized using a simple coprecipitation method.[19,28] An aqueous solution of metal chlorides ($InCl_3{\cdot}4H_2O$, $MnCl_2{\cdot}4H_2O$, $FeCl_2{\cdot}4H_2O$, $CoCl_2{\cdot}6H_2O$, $NiCl_2{\cdot}6H_2O$, or $CuCl_2{\cdot}4H_2O$; 1 M, 10 mL) was added to an aqueous solution of either $K_4[Fe(CN)_6]{\cdot}3H_2O$ or $K_3[Fe(CN)_6]$ (0.5 M, 20 mL). The mixture was stirred for 5 min. The resulting precipitates were collected by centrifugation, washed thrice with Milli-Q water and once with methanol, and then dried under vacuum overnight at 308 K. Mixed MHCFs, such as $K_2Mn_{0.4}Fe_{0.15}Co_{0.15}Ni_{0.15}Cu_{0.15}[Fe(CN)_6]$, were synthesized using the same procedure with a mixed metal chloride solution (1 M total, 10 mL).[33]

Preparation of RCO/TaON

TaON powder was synthesized according to a previously reported method as follows.[39] A mixture of $ZrO(NO_3)_2{\cdot}2H_2O$ (0.6 mmol) and Ta_2O_5 (3.0 mmol) was calcined in air at 1073 K for 2 h, followed by calcination at 1123 K for 15 h under NH_3 flow (12 mL min^{-1}). Characterization is provided in the SI (**Figures S1**: XRD and **S2**: UV–Vis diffuse reflectance spectrum). Rh-Cr mixed oxide particles (RCO) were loaded on TaON by a

View Article Online DOI: 10.1039/D6EE00066E

photodeposition method.[19,40] TaON particles were first suspended in an aqueous methanol solution (20 vol%) containing the required amount of $Na_3RhCl_6{\cdot}nH_2O$ and K_2CrO_4 (1.0 and 1.5 wt%, calculated as Rh and Cr with respect to TaON, respectively). The suspension was irradiated with visible light (λ > 400 nm) from a 300 W Xe lamp (LX-300F, Cermax) equipped with a cutoff filter (HOYA, L-42), while Ar gas was purged at 50 mL min^{-1} for 6 h. The resulting powder was collected by filtration and then dried under vacuum at 308 K overnight. The sample was denoted as RCO/TaON.

Modification of MHCF on RCO/TaON

MHCFs were loaded on RCO/TaON using the impregnation method.[19,28] MHCFs were dispersed in Milli-Q water (0.25 mmol/5 mL) and sonicated for 10 min, followed by stirring overnight to ensure complete dispersion. Thereafter, RCO/TaON particles were dispersed in the MHCF dispersion (Fe_C/Ta molar ratio = 0.1), and the mixture was stirred with a glass rod in an evaporation dish on a steam bath. The dried powder was heated at 373 K under Ar flow (20 mL min^{-1}) for 1 h. The sample was denoted as MHCF/RCO/TaON.

Synthesis of (Fe,Ru)O_x/Bi_4TaO_8Cl

Bi_4TaO_8Cl was synthesized by a flux method.[4,5] A precursor mixture of Bi_2O_3, BiOCl, and Ta_2O_5 (molar ratio $BiOCl:Bi_2O_3:Ta_2O_5$ = 1:1.5:0.5) was combined with a NaCl–CsCl mixed-flux (molar ratio NaCl:CsCl = 65:35 and flux:precursor = 5:95). The mixture was heated at 20 K h^{-1} to 1023 K and maintained for 15 h, then cooled naturally. The resulting yellow solid was washed with 500 mL of Milli-Q water, filtered by vacuum filtration, and then washed thrice on the filter with Milli-Q water (100 mL), followed by drying for 2 days (**Figures S1**: XRD and **S2**: UV–Vis diffuse reflectance spectrum). FeO_x and RuO_x species were loaded on Bi_4TaO_8Cl by the impregnation method.[41] Aqueous solutions of $FeCl_3{\cdot}6H_2O$ (250 mM) and $RuCl_3{\cdot}3H_2O$ (50 mM) were added to Bi_4TaO_8Cl particles (10 mol% of each relative to Bi_4TaO_8Cl) with 2 mL of Milli-Q water. The suspension was evaporated on a steam bath, and the obtained dark-green powder was subsequently calcined at 573 K for 1 h under an Ar flow (20 mL min^{-1}). The resulting sample is denoted as (Fe,Ru)O_x/Bi_4TaO_8Cl.

Synthesis of V-substituted Polyoxometalates

$K_6[\alpha\text{-}SiV^{IV}W_{11}O_{40}]{\cdot}11H_2O$ was synthesized via $K_8[\alpha\text{-}SiW_{11}O_{39}]{\cdot}13H_2O$ according to previously reported methods.[38,42] $K_7[\alpha\text{-}BV^{IV}W_{11}O_{40}]{\cdot}7H_2O$ was synthesized according to a previously reported method.[43] These POMs were denoted as SiV^{IV} and BV^{IV}, respectively. The hydration numbers were determined by TG-DTA measurement. See the SI for characterization (**Figures S3**: FT-IR and **S4**: cyclic voltammogram).

Characterization

The prepared samples were characterized by powder X-ray diffraction (XRD; Mini Flex II, Rigaku, X-ray source; Cu Kα) measurement, UV–Vis diffuse reflectance spectroscopy (V-650, JASCO), and scanning electron microscopy (SEM; NVision 40, Carl Zeiss-SIINT), scanning transmission electron microscopy coupled with energy-dispersive X-ray spectroscopy (STEM-EDS; JEOL, JEM-ARM200F). The samples were also characterized by ATR-FTIR (ATR; ATR Pro One, JASCO, FT-IR; FT-4200, JASCO) using a diamond prism. ATR-FTIR spectra were recorded against air as a background. For the POM samples, pellets were prepared by mixing the sample with KBr, and measurements were performed using the transmission mode. The absorption spectra of the solutions containing each POM were measured using a UV–Vis spectrometer (UV-1800, Shimadzu). The X-ray absorption fine structure (XAFS) measurements were performed at the BL12C beamlines of the Photon Factory (High Energy Accelerator Research Organization, Tsukuba, Japan). The X-ray absorption spectra were measured in transmission or fluorescence mode at room temperature using a Si(111) two-crystal monochromator.

Electrochemical measurement

The working electrode was prepared by coating the MHCF sample onto an FTO substrate. The sample powder was dispersed in a small amount of Milli-Q water or acetonitrile, and the dispersion was drop-cast onto the FTO substrate and wiped. This procedure was repeated once to ensure uniform coating. A three-electrode cell was employed, using an Ag/AgCl (3 M NaCl, BAS) as the reference electrode and a Pt coil as the counter electrode. Prior to measurements, the electrolyte solution was purged with Ar gas (100 mL min^{-1}). Potentials were controlled with a potentiostat (VersaSTAT 4, Princeton Applied Research).

Photocatalytic reaction

Photocatalytic reaction was evaluated in a Pyrex side-illuminated reaction vessel connected to a closed gas-circulation system. Visible light irradiation was provided by a 300 W Xe lamp equipped with an L-42 cutoff filter (λ > 400 nm). The reaction temperature was maintained at 288 K using a water bath. For the H_2 evolution half reaction, MHCF-modified or unmodified RCO/TaON powder (25 mg) was dispersed in aqueous KH_2PO_4 solution (0.05 M, 100 mL) containing SiV^{IV} or BV^{IV} as an electron donor (0.5 mM, 50 μmol). The suspension was thoroughly degassed and purged with Ar prior to irradiation. For the Zs-WS reaction, (Fe,Ru)O_x/Bi_4TaO_8Cl powder (50 mg) was added under the same conditions. The evolved H_2 and O_2 were quantified by a gas chromatograph (GC-8A, Shimadzu, TCD detector, MS 5A column, Ar carrier) directly connected to the closed gas-circulation system.

Results and Discussion

Physicochemical properties of MHCFs

All prepared MHCFs (Fe_C = Fe^{II} and M_N = Mn^{II}, Fe^{II}, Co^{II}, Ni^{II}, Cu^{II}, and In^{III}), including Mn-based high-entropy hexacyanoferrate (HEMHCF), were confirmed to be of single-phase by XRD patterns (**Figure 3(a)**). Most samples had a typical cubic structure, whereas MnHCF had a monoclinic phase that

View Article Online
DOI: 10.1039/D6EL00066E

was slightly distorted from the cubic structure.[23,44,45] SEM images showed particle sizes of several tens of nanometers (**Figure S5**), which aggregated into secondary particles with diameters of 100–200 nm. STEM-EDS mapping indicated that, after MHCF loading on RCO/TaON, MHCF was deposited on the RCO/TaON surface as a layer with a thickness of several tens of nanometers (**Figure S6**). **Figure 3(b)** shows ATR-FTIR spectra of reduced ($Fe_C = Fe^{II}$) and oxidized ($Fe_C = Fe^{III}$) forms. The observed IR absorption could be assigned to the C≡N stretching vibration of each MHCF. Apart from FeHCF, the oxidized forms of MHCF exhibited absorption peaks at higher wavenumbers than their reduced counterparts, consistent with increased back-donation upon oxidation. Some MHCFs ($M_N = Mn^{II}$, Ni^{II}, and In^{III}) exhibited only weak light absorption in the visible-light region (**Figure S7**), whereas those incorporating Fe^{II}, Cu^{II}, Co^{II}, and HEM exhibited strong absorption. Such absorption probably interfered with the absorption of the TaON photocatalyst (absorption edge at approximately 500 nm, **Figure S2**) when MHCFs were loaded onto its surface.

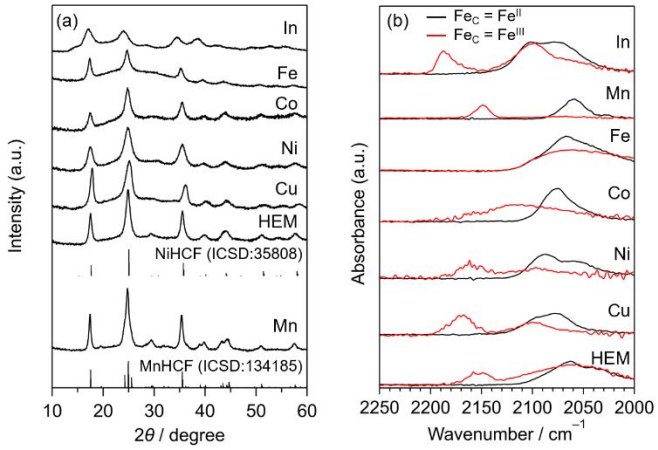

Figure 3. (a) XRD patterns of MHCFs ($Fe_C = Fe^{II}$) and (b) ATR-FTIR spectra of MHCFs (black lines: $Fe_C = Fe^{II}$ and red lines: $Fe_C = Fe^{III}$). The XRD pattern was indexed by reference to the ICSD database.[46]

Electrochemical property of MHCF

Figure 4 shows the cyclic voltammograms (CVs) of InHCF and FeHCF as examples of MHCF with redox-inactive M_N and redox-active M_N, respectively. CVs of other MHCFs are provided in **Figure S8**. InHCF and NiHCF exhibited simple CVs with a single redox pair originating from the $Fe_C^{III/II}$ (**Figure 4(a)**, **S8(b)**). The simple CV behavior of InHCF and NiHCF was reasonable considering the stable, essentially redox-inactive valence states of In^{III} and Ni^{II}.[30,47] Conversely, the CVs of FeHCF (Prussian blue), CoHCF, and CuHCF exhibited two redox couples (**Figure 4(b)**, **S8(c-f)**, **S9**). These multiple redox behaviors were assigned to $Fe_C^{III/II}$ and redox-active $M_N^{n+1/n+}$: in FeHCF, for example, the positive and negative redox couples correspond to $Fe^{III/II}$ coordinated to nitrogen ($Fe_N^{III/II}$) and carbon ($Fe_C^{III/II}$), respectively.[48,49]

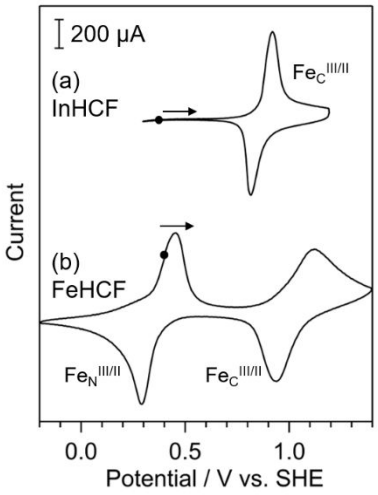

Figure 4. CVs of representative MHCFs with redox-inactive M_N ((a) InHCF) and redox-active M_N ((b) FeHCF) in 0.05 M KH_2PO_4 aqueous solution. Initial potential was set to the open rest potential, and scanning began in the anodic direction (50 mV s^{-1}).

Although previous reports revealed Mn in MnHCF to be redox-active and exhibit two distinct redox couples assigned to $Mn^{III/II}$ and $Fe_C^{III/II}$ in organic solution,[48,50] the CV of MnHCF measured in aqueous media (**Figure S8(c)**) did not display two distinct redox couples. Instead, its voltammetric profile more closely resembled those of MnO_2 and $MnCl_2$ in water (**Figure S10(a)**) than that of MnHCF in acetonitrile (**Figure S10(b),(c)**). These results suggest that the redox property of MnHCF in an aqueous medium is irreversible due to disproportionation of Mn^{III} species generated during the anodic scan: $2Mn^{III} + 2H_2O \rightarrow Mn^{II} + MnO_2 + 4H^+$.[51–54] Therefore, redox cycling of MnHCF has intrinsic instability when used in aqueous media; this phenomenon will be further discussed later. The redox potentials obtained by the CV in acetonitrile solution will be used hereafter, after appropriate conversion of potential to the SHE scale (**Figure S11**).[30,55]

HEMHCF (i.e., $K_2Mn_{0.4}Fe_{0.15}Co_{0.15}Ni_{0.15}Cu_{0.15}[Fe(CN)_6]$) displayed a single, well-defined redox couple (**Figure S12**), despite the presence of multiple redox-active M_N species. This convergence of redox features is commonly attributed to a so-called cocktail effect, in which the redox processes at the Fe_C and the M_N species proceed concurrently.[33,34,56]

Table 1 summarizes the half-wave potentials ($E_{1/2}$) of redox species in these MHCFs measured in 0.05 M KH_2PO_4 aqueous solution, except for that of MnHCF measured in 0.1 M KPF_6 acetonitrile solution. The assignment of redox couples for each MHCF was determined based on previous reports and additional experimental data provided in the SI.[48,57–60] Notably, all MHCFs displayed an irreversible reduction peak at approximately +0.1 V (vs. SHE, pH 4.5) to a greater or lesser extent (**Figure S8**). These peaks likely arise from the reduction of dissolved $[Fe^{III}(CN)_6]^{3-}$ as some of the oxidized MHCFs (e.g., $Fe_C = Fe^{III}$) are known to be partially soluble in water depending on the M_N species, which will be discussed in a later section.[61]

View Article Online
DOI: 10.1039/D5EE00066E

Table 1. Half-wave potentials ($E_{1/2}$) of MHCFs.

	$E_{1/2}$ / V vs. SHE	
M_N	$Fe_C^{III/II}$	$M_N^{n+1/n+}$
In[a]	+0.87	inactive
Mn[b]	+0.86	+1.12
Fe[a]	+1.03	+0.37
Co[a]	+0.84	+0.62
Ni[a]	+0.75	inactive
Cu[a]	+0.88	+0.24
HEM[a]	+0.86	+0.86

a. Measured in 0.05 M KH_2PO_4 aqueous solution (pH 4.5).
b. Measured in 0.1 M KPF_6 acetonitrile.

Dependence of M_N species on the photocatalytic half reaction of H_2 evolution

Figure 5(a) shows the time courses of H_2 evolution over various MHCF-modified RCO/TaON samples (10 mol% loading with respect to Fe_C relative to TaON), along with the unmodified RCO/TaON, in the presence of SiV^{IV} as an electron donor under visible-light irradiation. Except CuHCF, all MHCF modifications enhanced H_2 evolution relative to the unmodified RCO/TaON, on which the H_2 evolution rate gradually decreased, likely due to self-oxidation of TaON by photogenerated holes ($2N^{3-} + 6h^+ \rightarrow N_2$).[15] For M_N = Mn, Co, In, and HEM, higher H_2 evolution rates were observed in the initial stage (from 0.5 to 1.5 h), attributable to efficient hole consumption via $Fe_C^{III/II}$ and/or $M_N^{n+1/n+}$ redox cycles. Subsequently, H_2 evolution proceeded at a nearly steady rate, reaching approximately 25 µmol or higher, indicating that almost all the SiV^{IV} was oxidized to SiV^{V}. Specifically, the saturated amounts of H_2 on Mn and Co samples were obviously larger than 25 µmol, most probably due to the accumulation of oxidized species (i.e., Fe_C^{III} and/or M_N^{n+1}) within MHCF by photogenerated holes, which provided excess electrons. This occurrence is supported by H_2 generation under similar conditions but in the absence of POM (i.e., in pure water), as shown in **Figure 7(a)**, and will be discussed below. For MnHCF-modified RCO/TaON, the relationship between MnHCF loading amount and activity was investigated, and the rates showed little dependence on the loading amount over the range of 1–15 mol% (**Figure S13**). Although Fe- and Ni-modified samples initially displayed H_2 evolution rates comparable to that of unmodified TaON, their performance clearly improved after 1 h, indicating partial consumption of photogenerated holes through the oxidation of Fe_C^{II} and/or M_N^{n+}, which suppressed self-oxidation. By contrast, CuHCF modification produced a H_2 evolution profile similar to that of unmodified TaON.

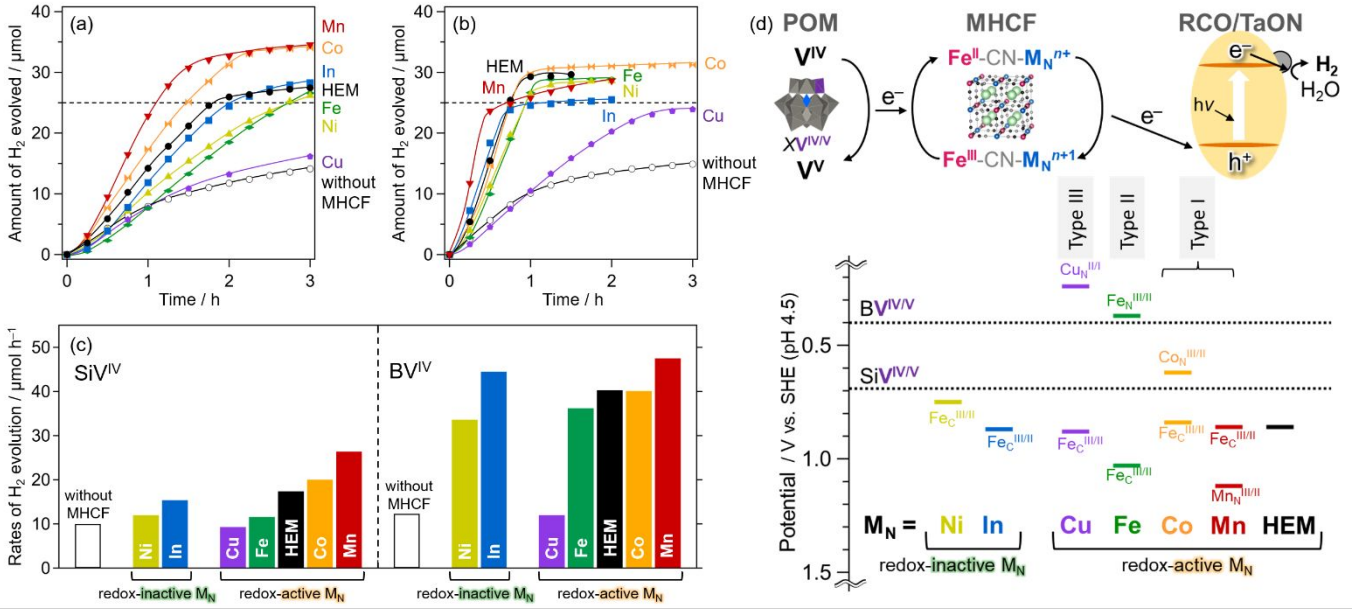

Figure 5. Time courses of H_2 evolution under visible-light irradiation over MHCF-modified or unmodified RCO/TaON in the presence of (a) 0.5 mM SiV^{IV} or (b) 0.5 mM BV^{IV} in aqueous KH_2PO_4 solution (50 mM KH_2PO_4, pH 4.5, 100 mL). Dotted lines show the amount of H_2 evolution corresponding to one electron donation by SiV^{IV} or BV^{IV}. (c) Rates of the H_2 evolution half reaction for each combination. (d) Schematic illustration of the half reaction of H_2 evolution over MHCF-modified RCO/TaON using POM as an electron donor and potential relationship between V-POMs and MHCFs.

Figure 5(b) shows H_2 evolution in the presence of BV^{IV} as an electron donor. All MHCF-modified samples, including FeHCF and NiHCF systems, exhibited enhancement in H_2 evolution from the initial stage of irradiation. CuHCF suppressed the rate decrease observed for unmodified RCO/TaON, unlike the SiV^{IV} system, indicating a functional $Fe_C^{III/II}$ redox cycle in this case, although the overall H_2 evolution enhancement remained limited.

Figure 5(c) summarizes the maximum H_2 evolution rates obtained with both POMs. All MHCF-modified samples exhibited higher rates with BV^{IV} than with SiV^{IV}, except for CuHCF, consistent with the more negative potential of the $BV^{V/IV}$

View Article Online
DOI: 10.1039/D6EL00066E

(+0.40 V) compared with that of $SiV^{V/IV}$ (+0.69 V), which afforded a larger driving force for electron transfer from the POM to MHCF.[28]

Relationship between H_2 evolution rate and redox properties of MHCFs depending on M_N

Figure 5(d) summarizes the redox potentials of MHCFs and POMs. Given the valence band maximum (VBM) of TaON (approximately +1.9 V vs. SHE at pH 4.5), the photogenerated holes could oxidize all the redox-active species in the MHCFs (Fe_C^{II} and M_N). For MHCFs containing redox-inactive M_N species (i.e., In, Ni), the observed H_2 evolution could be rationalized by the potential difference between $Fe_C^{III/II}$ and POMs, with larger differences corresponding to higher H_2 evolution rates.[28] However, for MHCFs with redox-active M_N species (Mn, Co, Fe, and Cu), the H_2 evolution activity can be classified into three distinct types.

Type I (M_N = Mn, Co): Both MnHCF and CoHCF exhibit markedly enhanced H_2 evolution with both POMs, with higher rates observed for BV^{IV} than for SiV^{IV}, similar to the case of InHCF and NiHCF. In these materials, the redox-active species exhibit redox potentials more positive than those of either POM, thereby allowing electron injection from the reduced POMs to the oxidized MHCF species. Although the redox potential of $Co^{III/II}$ in CoHCF (+0.62 V) is slightly more negative than that of $SiV^{V/IV}$ (+0.69 V), electron transfer remains thermodynamically suitable when considering that $E_{1/2}$ values are defined under equimolar oxidized and reduced conditions. Overall, oxidation of the redox-active species (both Fe_C and M_N) by photogenerated holes, followed by electron injection from the POMs, provides a consistent explanation for the high H_2 evolution rates observed.

Type II (M_N = Fe): FeHCF markedly enhances H_2 evolution in the presence of BV^{IV}, whereas only a limited enhancement is observed with SiV^{IV}. FeHCF contains two redox-active species, $Fe_C^{III/II}$ (+1.03 V) and $Fe_N^{III/II}$ (+0.37 V). In the presence of BV^{IV} as an electron donor, both oxidized Fe species are thermodynamically reducible, resulting in a substantial enhancement of H_2 evolution. By contrast, SiV^{IV} enables the reduction of only Fe_C^{III}, whereas the $Fe_N^{III/II}$ remains unreduced (**Figure 6(a)**). The persistence of Fe_N^{III} facilitates electron trapping from photoexcited TaON, thereby promoting electron-hole recombination and limiting H_2 evolution (**Figure 6(b)**). This occurs despite partial hole scavenging, which suppresses self-oxidation of the TaON.

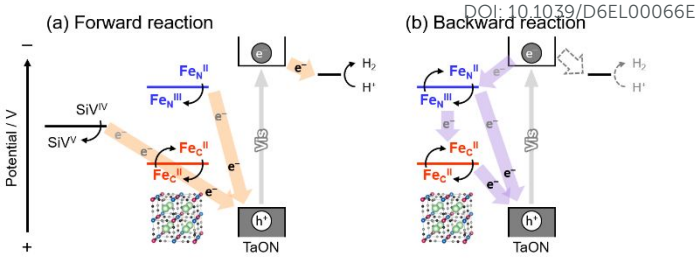

Figure 6. Proposed schematic of (a) forward reaction where SiV^{IV} is oxidized via $Fe_C^{III/II}$ in FeHCF, and (b) backward reaction where the excited electrons and holes recombine via $Fe_N^{III/II}$ in FeHCF.

Type III (M_N = Cu): In CuHCF, the $Cu^{II/I}$ redox potential is more negative than that of $BV^{V/IV}$, causing photogenerated electrons in TaON to reduce Cu^{II} instead of producing H_2. Therefore, H_2 evolution was only slightly enhanced with either electron donor. These results for FeHCF and CuHCF highlight an important design principle for H_2 evolution using MHCF modifiers, i.e., the presence of redox species with potentials significantly more negative than that of the electron donor is detrimental.

As for the Mn-based high-entropy MHCF (HEMHCF; $K_2Mn_{0.4}Fe_{0.15}Co_{0.15}Ni_{0.15}Cu_{0.15}[Fe(CN)_6]$), the H_2 evolution rate with HEMHCF is similar to that with InHCF, which possess similar redox potential, in both cases with SiV^{IV} and BV^{IV}.

As mentioned above, several MHCFs (FeHCF, CoHCF, CuHCF, and HEMHCF) exhibit strong absorption in the visible region (**Figure S7**), partially overlapping with that of TaON. Although the MHCFs are modified as thin layers on the TaON surface (**Figure S6**), light shielding by the MHCFs may contribute to the apparent decrease in H_2 evolution activity.[19,28] However, because the observed activity trends (**Figure 5, S14, S15**) cannot be rationalized by differences in the extent of absorption, light shielding effect is unlikely to be the dominant factor in this system.

Stability test of MHCFs during H_2 evolution reaction

As suggested by the CVs in **Figure S10,** MnHCF is partially susceptible to oxidative decomposition. To evaluate the structural stability of MHCFs, especially their oxidized forms, MHCF-modified RCO/TaON particles dispersed in Milli-Q water were irradiated with visible light. Structural changes were examined by comparing the C≡N stretching vibrations of the sample and $[Fe^{III}(CN)_6]^{3-}$ formation in aqueous solution before and after irradiation. Under irradiation, all MHCFs produced 3–20 μmol of H_2 (**Figure 7(a)**). For FeHCF, CoHCF, NiHCF, CuHCF, and HEMHCF modified TaON, the IR absorption peaks shifted to higher wavenumbers after irradiation (**Figure 7(b)**), indicating the oxidation of Fe_C and/or M_N species by photogenerated holes (**Figure 3(b)**). The decrease in the intensity of peaks corresponding to the reduced form suggests the formation of oxidized forms and partial dissolution and/or decomposition of MHCFs. For MnHCF, the disappearance of the IR absorption after irradiation indicated that the compound was completely dissolved and/or decomposed. This was also indicated by Fe K-edge X-ray absorption near edge structure (XANES) (**Figure 7(c)**), where the spectrum of MnHCF/RCO/TaON after

View Article Online
DOI: 10.1039/D6EE00066E

irradiation differed from that of pristine MnHCF and was similar to that of Fe_2O_3. STEM-EDS elemental mapping of MnHCF/RCO/TaON after photoirradiation (**Figure 7(e)**) revealed aggregation of Mn species on the RCO/TaON surface, as well as spatial separation of Mn and Fe species. This further suggests the decomposition of MnHCF. In addition, the absorption attributable to $[Fe^{III}(CN)_6]^{3-}$ was observed in the solutions of all MHCF-modified samples except CuHCF; the strongest intensity was observed for MnHCF (**Figure 7(d)**). Note that MnHCF/RCO/TaON evolved a larger amount of H_2 (approximately 20 μmol) than the other MHCF-modified samples (**Figure 7(a)**), indicating that both Fe_C^{II} and Mn^{II} species were oxidized.

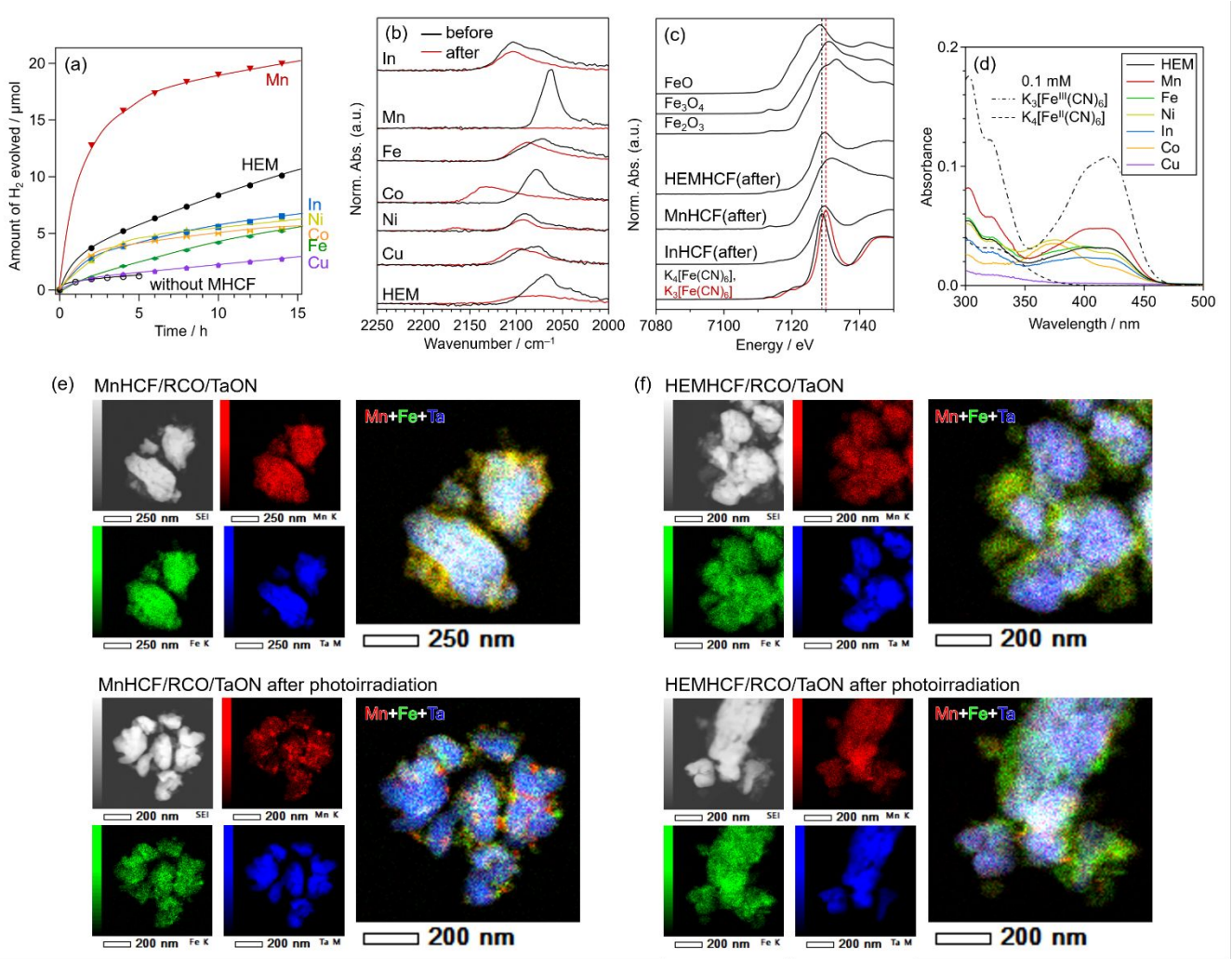

Figure 7. (a) Time course of H_2 evolution under visible-light irradiation over MHCF-modified or unmodified RCO/TaON in Milli-Q water. (b) Normalized ATR-FTIR spectra of MHCF/RCO/TaON before and after irradiation. (c) Fe K-edge XANES of MHCF/RCO/TaON after photoirradiation, together with the reference samples. (d) UV–Vis absorption spectra of the reaction solution after visible-light irradiation. STEM-EDS elemental mappings images of (e) MnHCF/RCO/TaON and (f) HEMHCF/RCO/TaON before and after photoirradiation in pure water. The distributions of Mn, Fe, and Ta are shown in red, green, and blue, respectively.

Stirring MHCF particles with reduced (Fe_C^{II}) or oxidized (Fe_C^{III}) species in aqueous solution in the dark for 20 min resulted in increased absorption assigned to the iron cyanide complex for all MHCFs to varying extents (**Figure S16**). Most MHCFs displayed higher solubility of the oxidized forms (Fe_C^{III}) than that of the reduced forms (Fe_C^{II}),[61] and this tendency was particularly pronounced for MnHCF. These results indicate that MnHCF is susceptible to oxidative dissolution and/or decomposition, consistent with the substantial formation of $[Fe^{III}(CN)_6]^{3-}$ under photoirradiation (**Figure 7(d)**). This limited durability is also consistent with previous reports showing that Mn^{III}-induced Jahn–Teller distortion and related structural phase transitions during redox cycling reduce redox reversibility.[33,55] Assuming that MnO_x species are formed through MnHCF decomposition, we examined whether these MnO_x species contribute to the H_2 evolution activity. In the presence of Si^{IV} as an electron donor, MnO_x/RCO/TaON exhibited a lower H_2 evolution rate than unmodified RCO/TaON (**Figure S17**), indicating that MnO_x species are not responsible for the enhanced activity of MnHCF/RCO/TaON.

Conversely, the amount of $[Fe^{III}(CN)_6]^{3-}$ after irradiation was lower for HEMHCF than that for MnHCF (**Figure 7(d)**), consistent with the lower solubility of oxidized HEMHCF compared with that of MnHCF (**Figure S16(b)**). The IR absorption corresponding

View Article Online
DOI: 10.1039/D6EL00066E

to the cyanide ligands of HEMHCF shifted to higher wavenumbers (**Figure 7(b)**), indicating the occurrence of oxidation. Furthermore, the XANES spectrum of HEMHCF/RCO/TaON after photoirradiation was identical to that of $K_3[Fe^{III}(CN)_6]$ (**Figure 7(c)**). STEM-EDS elemental mapping (**Figure 7(f)**) further showed that Mn and Fe species were closely located. These results indicate that the structure of the surface-loaded HEMHCF is largely retained after photoirradiation. The amount of H_2 evolved from HEMHCF/RCO/TaON was approximately 10 μmol (**Figure 7(a)**), which reasonably corresponded to the total amount of electron-donating species in HEMHCF (Mn^{II}, Fe^{II}, and Co^{II}; estimated to be approximately 17 μmol in total). These results suggest that incorporation into the high-entropy structure enhances the durability of HEMHCF against decomposition. The enhanced durability of HEMHCF is consistent with previous reports, where partial substitution of Mn in Mn-based hexacyanoferrates mitigates Mn^{III}-induced structural changes and improves redox reversibility.[33]

Zs-WS using MHCF-modified TaON as HEP

Finally, MHCF/RCO/TaON was coupled with an OEP ($(Fe,Ru)O_x/Bi_4TaO_8Cl$)[41] for Zs-WS using $SiV^{V/IV}$ as a shuttle redox mediator (**Figure 8(a)**). TaON without MHCF rapidly deactivated, certainly due to the self-oxidation.[15] By contrast, MHCF-modified TaON initially exhibited relatively steady H_2 and O_2 evolution, indicating that Fe_C^{II} and/or redox-active M_N species scavenged photogenerated holes and promoted SiV^{IV} oxidation (**Figure 8(a)**). Among these, MnHCF/RCO/TaON displayed relatively higher gas evolution rates during the first 5 h than other MHCFs (**Figure 8(b)**). However, the gas evolution rates gradually decreased after the initial 5 h. A comparable decrease was observed for the other MHCF-modified samples, apart from HEMHCF, most likely due to dissolution and/or oxidative decomposition under the reaction conditions. By contrast, HEMHCF/RCO/TaON, maintained its activity over a longer period (**Figure 8(c)**), demonstrating that the combination of its oxidative durability and its ability to efficiently oxidize the redox mediator enhanced hole consumption and effectively suppressed photocatalyst deactivation.

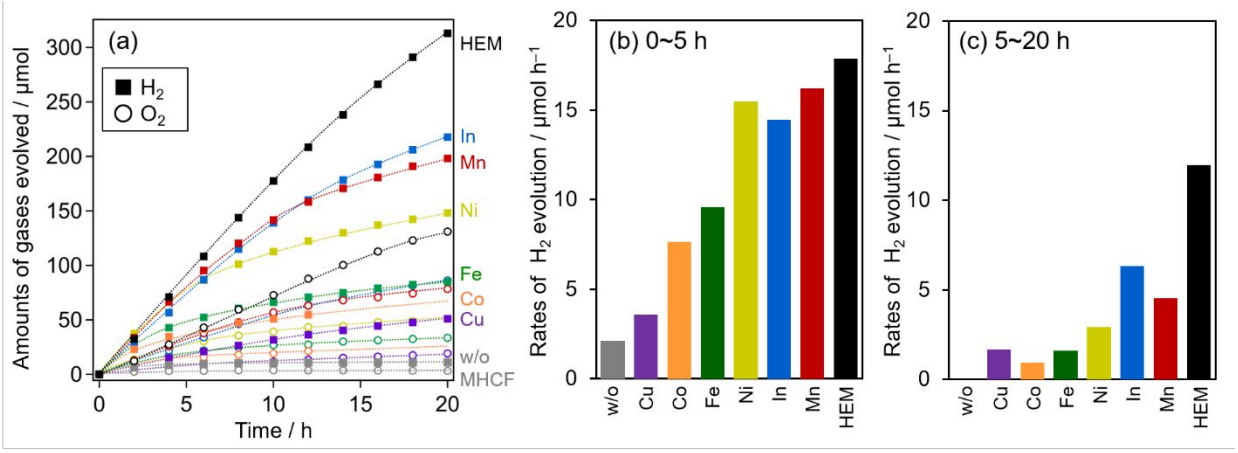

Figure 8. (a) Time courses of H_2 and O_2 evolution over 25 mg of H_2-evolving photocatalyst (MHCF/RCO/TaON or RCO/TaON) and 50 mg of O_2-evolving photocatalyst ($(Fe,Ru)O_x/Bi_4TaO_8Cl$) in the presence of 0.5 mM SiV^{IV} in aqueous KH_2PO_4 solution (50 mM, pH 4.5). Rates of H_2 evolution during the (b) first 5 h (filled) and (c) 15–20 h (open).

Conclusions

This study classified the effects of M_N species in MHCFs on hole extraction from HEP (RCO/TaON) in Zs-WS. MHCFs with redox-inactive M_N species (i.e., In, Ni) exhibited a simple $Fe_C^{III/II}$-mediated behavior, in which enhancement of H_2 evolution scaled with the potential difference between the POM electron donor and the Fe_C redox couple. MHCFs with redox-active M_N species could be further classified into three types. Type I included MHCFs with M_N = Mn or Co, which comprised beneficial dual redox sites (Fe_C and M_N), both of whose potentials were more positive than those of the POM electron donors. The M_N species of this type, as well as Fe_C, could participate in hole capture, regeneration by the electron donor, and a marked enhancement of H_2 evolution. Type II included FeHCF, where enhancement in H_2 evolution was observed only with a sufficiently reducing donor (BV^{IV}), because both Fe_C and Fe_N sites could participate in forward redox cycling. By contrast, with a weaker donor (SiV^{IV}), the Fe_N site remained oxidized and induced backward electron transfer, suppressing the apparent activity. Type III included CuHCF, where the redox potential of $Cu^{II/I}$ was much more negative than that of electron donors and preferentially traps photogenerated electrons, resulting in negligible improvement in H_2 evolution. Overall, redox-active M_N species could promote oxidation of the redox mediator only when the redox potential of M_N was more positive than that of the electron donor.

Among the tested MHCFs, MnHCF exhibited the highest H_2 evolution activity but suffered from oxidative dissolution

View Article Online
DOI: 10.1039/D6EL00066E

and/or decomposition, causing a marked decay in activity during the Zs-WS reaction. Accelerating electron donation from the redox couple should be an effective strategy to prevent dissolution of MHCFs in their highly oxidized states. In addition, high-entropy design was shown to be a promising approach for fundamentally improving the oxidative stability. Mn-based high-entropy MHCF incorporating multiple M_N species stabilized Mn redox cycling, leading to minimized decay in Zs-WS activity. These results demonstrate that high-entropy engineering of the cocatalyst enables the enhancement of both activity and durability for long-term Zs-WS systems.

Author contributions

Harutaka Ninomiya: Conceptualization; Data curation; Formal Analysis; Investigation; Writing – original draft. **Osamu Tomita**: Funding acquisition; Investigation; Writing – review & editing. **Hajime Suzuki**: Investigation; Writing – review & editing. **Akinobu Nakada**: Investigation; Writing – review & editing. **Rie Haruki**: Data curation; Writing – review & editing. **Shunsuke Nozawa**: Data curation; Writing – review & editing. **Ryu Abe**: Funding acquisition; Methodology; Project administration; Supervision; Writing – review & editing.

Conflicts of interest

There are no conflicts to declare.

Data availability

Data are available within the article or its supplementary information (SI). Supplementary information: includes additional figures supporting the main findings. See DOI: XXX

Acknowledgements

This work was supported by "JSPS KAKENHI" (JP24K01528, JP25K01877, and JP25KJ1452), "Tokyo Ohka Foundation for the Promotion of Science and Technology" and "Advanced Research Infrastructure for Materials and Nanotechnology in Japan (ARIM)" of the Ministry of Education, Culture, Sports, Science and Technology (MEXT) (JPMXP1226KT0011). XAFS experiments were performed with the approval of the Photon Factory Program Advisory Committee (Proposal No.2024G638 and 2024G147). The authors are indebted to the technical division of the Institute for Catalysis, Hokkaido University, for their help in building the experimental equipment. The crystal structures were illustrated using the VESTA program.[62]

Broader Context Statement

Water and sunlight are abundant and globally available resources, making solar water splitting an attractive route to sustainable hydrogen production. Among the proposed approaches, particulate Z-scheme systems are particularly appealing because they can enable scalable solar H_2 production using dispersed semiconductor materials and simple reactor configurations. However, their performance is often limited not only by the semiconductor photocatalysts themselves, but also by inefficient interfacial electron transfer between aqueous redox mediators and photocatalyst surfaces. Nevertheless, the design of cocatalysts for redox-mediator oxidation has received far less attention than that for water reduction or oxidation. In this work, we show that metal hexacyanoferrates can serve as tunable mediator-oxidation cocatalysts, and that their redox potentials critically govern forward charge extraction and backward electron transfer. We further demonstrate that high-entropy compositional design improves durability while retaining function. Together, these findings establish a redox-potential-based design principle for mediator oxidation and provide a general framework for engineering interfacial redox selectivity and durability in solar-to-fuel conversion systems.

References

1 B. A. Pinaud, J. D. Benck, L. C. Seitz, A. J. Forman, Z. Chen, T. G. Deutsch, B. D. James, K. N. Baum, G. N. Baum, S. Ardo, H. Wang, E. Miller and T. F. Jaramillo, *Energy Environ. Sci.*, 2013, **6**, 1983.
2 Y. Wang, H. Suzuki, J. Xie, O. Tomita, D. J. Martin, M. Higashi, D. Kong, R. Abe and J. Tang, *Chem. Rev.*, 2018, **118**, 5201–5241.
3 R. Abe, K. Sayama, K. Domen and H. Arakawa, *Chem. Phys. Lett.*, 2001, **344**, 339–344.
4 S. Chang, L. Shi, J. Yu, R. Wang, X. Xu and G. Liu, *Appl. Catal. B Environ.*, 2023, **328**, 122541.
5 K. Ogawa, A. Nakada, H. Suzuki, O. Tomita, M. Higashi, A. Saeki, H. Kageyama and R. Abe, *ACS Appl. Mater. Interfaces*, 2019, **11**, 5642–5650.
6 C. Zhang, X. Liang, W. Xing, K. Liu, Z. Zheng, S. Wang, G. Zhang and X. Wang, *J. Am. Chem. Soc.*, 2026, **148**, 17272–17282.
7 J. Yang, D. Wang, H. Han and C. Li, *Acc. Chem. Res.*, 2013, **46**, 1900–1909.
8 M. G. Walter, E. L. Warren, J. R. McKone, S. W. Boettcher, Q. Mi, E. A. Santori and N. S. Lewis, *Chem. Rev.*, 2010, **110**, 6446–6473.
9 T. Takata, J. Jiang, Y. Sakata, M. Nakabayashi, N. Shibata, V. Nandal, K. Seki, T. Hisatomi and K. Domen, *Nature*, 2020, **581**, 411–414.
10 Q. Wang, D. Zheng, Z. Pan, W. Xing, S. Wang, Y. Hou, M. Anpo and G. Zhang, *Adv. Funct. Mater.*, 2025, **35**, 2501889.
11 R. Abe, M. Higashi and K. Domen, *ChemSusChem*, 2011, **4**, 228–237.
12 K. Murofushi, K. Ogawa, H. Suzuki, R. Sakamoto, O. Tomita, K. Kato, A. Yamakata, A. Saeki and R. Abe, *J. Mater. Chem. A*, 2021, **9**, 11718–11725.
13 A. Iwase, H. Kato and A. Kudo, *Chem. Lett.*, 2005, **34**, 946–947.
14 M. Qureshi, T. Shinagawa, N. Tsiapis and K. Takanabe, *ACS Sustainable Chem. Eng.*, 2017, **5**, 8079–8088.
15 R. Abe, M. Higashi and K. Domen, *J. Am. Chem. Soc.*, 2010, **132**, 11828–11829.
16 A. Harriman, I. J. Pickering, J. M. Thomas and P. A. Christensen, *J. Chem. Soc., Faraday Trans. 1*, 1988, **84**, 2795.
17 Y. Iwase, O. Tomita, M. Higashi, A. Nakada and R. Abe, *Sustainable Energy Fuels*, 2019, **3**, 1501–1508.
18 Y. Iwase, O. Tomita, M. Higashi and R. Abe, *Sustainable Energy Fuels*, 2017, **1**, 748–754.
19 H. Matsuoka, T. Inoue, H. Suzuki, O. Tomita, S. Nozawa, A. Nakada and R. Abe, *Solar RRL*, 2023, **7**, 2300431.

View Article Online
DOI: 10.1039/D5EE00066E

20 T. Shirakawa, M. Higashi, O. Tomita and R. Abe, *Sustainable Energy Fuels*, 2017, **1**, 1065–1073.
21 Y. Kageshima, Y. Gomyo, H. Matsuoka, H. Inuzuka, H. Suzuki, R. Abe, K. Teshima, K. Domen and H. Nishikiori, *ACS Catal.*, 2021, **11**, 8004–8014.
22 H. Matsuoka, M. Higashi, A. Nakada, O. Tomita and R. Abe, *Chem. Lett.*, 2018, **47**, 941–944.
23 J. F. Keggin and F. D. Miles, *Nature*, 1936, **137**, 577–578.
24 F. Scholz and A. Dostal, *Angew. Chem. Int. Ed. Engl.*, 1996, **34**, 2685–2687.
25 A. Gotoh, H. Uchida, M. Ishizaki, T. Satoh, S. Kaga, S. Okamoto, M. Ohta, M. Sakamoto, T. Kawamoto, H. Tanaka, M. Tokumoto, S. Hara, H. Shiozaki, M. Yamada, M. Miyake and M. Kurihara, *Nanotechnology*, 2007, **18**, 345609.
26 E. Kholoud, H. Watanabe, A. Takahashi, M. M. Emara, B. A. Abd-El-Nabey, M. Kurihara, K. Tajima and T. Kawamoto, *J. Mater. Chem. C*, 2017, **5**, 8921–8926.
27 M. Zentkova and M. Mihalik, *Crystals*, 2019, **9**, 112.
28 H. Ninomiya, O. Tomita, H. Suzuki, A. Nakada and R. Abe, *ACS Materials Lett.*, 2024, **6**, 2474–2478.
29 K. Hurlbutt, S. Wheeler, I. Capone and M. Pasta, *Joule*, 2018, **2**, 1950–1960.
30 Y. Lu, L. Wang, J. Cheng and J. B. Goodenough, *Chem. Commun.*, 2012, **48**, 6544–6546.
31 L. Wang, Y. Lu, J. Liu, M. Xu, J. Cheng, D. Zhang and J. B. Goodenough, *Angew. Chem., Int. Ed.*, 2013, **52**, 1964–1967.
32 B. Liu, Q. Zhang, L. Zhang, X. Yong, L. Li and C. Wang, *Energy Storage Mater.*, 2024, **66**, 103221.
33 Y. Ma, Y. Hu, Y. Pramudya, T. Diemant, Q. Wang, D. Goonetilleke, Y. Tang, B. Zhou, H. Hahn, W. Wenzel, M. Fichtner, Y. Ma, B. Breitung and T. Brezesinski, *Adv. Funct. Mater.*, 2022, **32**, 2202372.
34 Y. Ma, Y. Ma, S. L. Dreyer, Q. Wang, K. Wang, D. Goonetilleke, A. Omar, D. Mikhailova, H. Hahn, B. Breitung and T. Brezesinski, *Adv. Mater.*, 2021, **33**, 2101342.
35 O. Tomita, H. Naito, A. Nakada, M. Higashi and R. Abe, *Sustainable Energy Fuels*, 2022, **6**, 664–673.
36 Y. Iwase, O. Tomita, H. Naito, M. Higashi and R. Abe, *J. Photochem. Photobiol., A*, 2018, **356**, 347–354.
37 K. Tsuji, O. Tomita, M. Higashi and R. Abe, *ChemSusChem*, 2016, **9**, 2201–2208.
38 O. Tomita, K. Tachizawa, T. Kido, H. Suzuki, A. Nakada and R. Abe, *Adv. Funct. Mater.*, 2025, **35**, 2505908.
39 K. Maeda, H. Terashima, K. Kase, M. Higashi, M. Tabata and K. Domen, *Bull. Chem. Soc. Jpn.*, 2008, **81**, 927–937.
40 K. Maeda, D. Lu, K. Teramura and K. Domen, *Energy Environ. Sci.*, 2010, **3**, 470–477.
41 A. Nakada, H. Suzuki, J. J. M. Vequizo, K. Ogawa, M. Higashi, A. Saeki, A. Yamakata, H. Kageyama and R. Abe, *ACS Appl. Mater. Interfaces*, 2019, **11**, 45606–45611.
42 A. Tézé, G. Hervé, R. G. Finke and D. K. Lyon, in *Inorganic Syntheses*, John Wiley & Sons, Ltd, 1990, pp. 85–96.
43 J. J. Altenau, M. T. Pope, R. A. Prados and Hyunsoo. So, *Inorg. Chem.*, 1975, **14**, 417–421.
44 L. Li, Z. Hu, Y. Lu, C. Wang, Q. Zhang, S. Zhao, J. Peng, K. Zhang, S.-L. Chou and J. Chen, *Angewandte Chemie International Edition*, 2021, **60**, 13050–13056.
45 M. Fiore, S. Wheeler, K. Hurlbutt, I. Capone, J. Fawdon, R. Ruffo and M. Pasta, *Chem. Mater.*, 2020, **32**, 7653–7661.
46 D. Zagorac, H. Müller, S. Ruehl, J. Zagorac and S. Rehme, *J. Appl. Cryst.*, 2019, **52**, 918–925.
47 L. Chen, H. Shao, X. Zhou, G. Liu, J. Jiang and Z. Liu, *Nat. Commun.*, 2016, **7**, 11982.
48 B. Wang, Y. Han, X. Wang, N. Bahlawane, H. Pan, M. Yan and Y. Jiang, *iScience*, 2018, **3**, 110–133.
49 D. Ellis, M. Eckhoff and V. D. Neff, *J. Phys. Chem.*, 1981, **85**, 1225–1231.
50 J. Song, L. Wang, Y. Lu, J. Liu, B. Guo, P. Xiao, J.-J. Lee, X.-Q. Yang, G. Henkelman and J. B. Goodenough, *J. Am. Chem. Soc.*, 2015, **137**, 2658–2664.
51 R. Benedek, *J. Phys. Chem. C*, 2017, **121**, 22049–22053.
52 J. C. Hunter, *J. Solid State Chem.*, 1981, **39**, 142–147.
53 H. N. Wilson and J. G. M. Bremner, *Q. Rev. Chem. Soc.*, 1948, **2**, 1–24.
54 H. G. Dion and P. J. G. Mann, *J. Agric. Sci.*, 1946, **36**, 239–245.
55 X. Bie, K. Kubota, T. Hosaka, K. Chihara and S. Komaba, *J. Mater. Chem. A*, 2017, **5**, 4325–4330.
56 C. Li, Y. Xiao, D. Zhang, X. Yuan, J. Xiao, Y. Zhao, H. Gao and H. Liu, *Batteries*, 2025, **11**, 328.
57 D. R. Shankaran and S. S. Narayanan, *Fresenius J. Anal. Chem.*, 1999, **364**, 686–689.
58 O. Makowski, J. Stroka, P. J. Kulesza, M. A. Malik and Z. Galus, *J. Electroanal. Chem.*, 2002, **532**, 157–164.
59 M. Giorgetti, L. Guadagnini, D. Tonelli, M. Minicucci and G. Aquilanti, *Phys. Chem. Chem. Phys.*, 2012, **14**, 5527.
60 L. Guadagnini, D. Tonelli and M. Giorgetti, *Electrochimica Acta*, 2010, **55**, 5036–5039.
61 X. Lamprecht, F. Speck, P. Marzak, S. Cherevko and A. S. Bandarenka, *ACS Appl. Mater. Interfaces*, 2022, **14**, 3515–3525.
62 K. Momma and F. Izumi, *J. Appl. Cryst.*, 2011, **44**, 1272–1276.

View Article Online
DOI: 10.1039/D6EL00066E

Data Availability Statement

Supplementary information (SI) available: X-ray diffraction patterns, UV–Vis diffuse reflectance spectra, FT-IR spectra, cyclic voltammograms, SEM images, UV–Vis absorption spectra, and photocatalytic activity data.